Ionospheric Scintillation Observation Using Space-Borne Synthetic Aperture Radar Data

S. Mohanty[1], G. Singh[1] iD, C. S. Carrano[2] iD, and S. Sripathi[3] iD

[1]Centre of Studies in Resources Engineering, Indian Institute of Technology Bombay, Mumbai, Maharashtra, India, [2]Institute for Scientific Research, Boston College, Boston, MA, USA, [3]Indian Institute of Geomagnetism, Navi Mumbai, Maharashtra, India

Abstract Networks of ground-based global navigation satellite system (GNSS) receivers have been widely used to monitor scintillation caused by irregularities in the disturbed ionosphere. Due to the relative sparseness of such networks, however, scintillation measurements are lacking in many regions of the globe, and even in well-instrumented geographic areas, the spacing between receivers is often too large to study the systematic spatial changes in scintillation characteristics, for example, across the equatorial anomaly region. This paper discusses the potential of studying ionospheric scintillations using low-frequency synthetic aperture radar (SAR). It compares standard metrics of scintillation including the amplitude scintillation index S_4 and vertically integrated strength of turbulence $C_k L$, from GNSS and SAR, on two different dates with varying ionospheric conditions. For this study, polarimetric L-band SAR images acquired from the Phased Array-type L-band Synthetic Aperture Radar sensor onboard the Advanced Land Observational Satellite-2 have been used. A number of GNSS satellites also observed the particular scintillation event that was encountered by SAR on the night of 23 March 2015 over the southern and mid-central India. The S_4 index derived from SAR are computed using previously published techniques in terms of radar backscatter ($\sigma°$) enhancement and the image contrast. The results show a favorable correlation with the GNSS observations. Along with accurate information about satellite geometry and operating frequency, few spectral properties of ionospheric irregularities, such as spectral index, anisotropy, and outer scale, have been assumed from historically available low-latitude scintillation observations to calculate the turbulence strength parameter. The results are well corroborated by measurements from four GNSS stations in India, thus demonstrating the utility of the SAR measurements in augmenting and complementing the ionospheric scintillation diagnostics available from GNSS.

1. Introduction

In the past decade or so, Earth observation applications using space-borne microwave remote sensing, and synthetic aperture radar (SAR) sensors, in particular, have increased manifold. These include climate and coastal zone monitoring, land use, forest and agriculture, and natural resources exploration applications (Moreira, 2013). Among them, forest and biomass monitoring has become a promising application for global climate change prediction studies using low frequency L- and P-band SAR sensors (Ningthoujam et al., 2016; Tong Minh et al., 2016). However, these sensor acquisitions are affected by the ionosphere, which may be a limiting factor under some circumstances, depending on mission design (Ishimaru et al., 1999; Xu et al., 2004). In addition to this, ionospheric scintillations have detrimental effects on SAR propagation causing signal degradation, loss of coherence, phase errors (Alizadeh et al., 2013), defocusing (Belcher, 2008; Van de Kamp et al., 2009), and striping (Shimada et al., 2008).

Ionospheric scintillation is defined as modulations of the amplitude and/or phase of the signal waveform due to electron density irregularities in the ionosphere. These irregularities cause random modulations of the original wavefront that affect signal phase (Belcher & Rogers, 2008) and/or amplitude (Belcher & Cannon, 2014), angle of arrival, and polarization (Priyadarshi, 2015). This occurs mostly in the post-sunset equatorial belt due to plasma interchange instabilities (Carter et al., 2018; Hysell et al., 2017; Somayajulu et al., 1984) that result from the rapid recombination of free-electrons in the bottomside ionosphere after sunset. Less severe scintillation also occurs in the high latitude regions due to polar patches and auroral precipitation (Prikryl et al., 2016; Jin et al., 2017).

In the equatorial region, ionospheric irregularities are viewed as rod-like structures aligned with the geomagnetic field lines while at high latitudes they often manifest as sheet-like structures. As the low-frequency SAR satellite ascends or descends in latitude over the low-latitude region, the wave undergoes two processes. First, the transmitted wave interacts with the irregularities, followed by a downward propagation of the resulting modulated wavefront to the ground during which diffraction effects accumulate (Carrano et al., 2012). The distorted wavefront interacts with the targets on the ground and then traverses the ionosphere a second time. Note that the accumulated modulations caused by the first ionospheric traversal and the ground interaction are modulated by the ionosphere a second time as the wave returns to the receiver. Depending upon the size of the irregularities compared to the first Fresnel scale $(\lambda z)^{1/2}$ (where λ represents the signal wavelength and z is the distance between the irregularity layer and the target), the wavefront can undergo primarily refraction or diffraction (Briggs, 1975). Scintillation structures with characteristic scale larger than the geometry-dependent Fresnel scale tend to impart phase but not amplitude modulation, whereas ionospheric structure smaller than the Fresnel scale imparts both phase and amplitude modulations (Xu et al., 2004). When the variations in phase become $\sim\pi/4$ radians, scintillations reduce the image focus and contrast. Such instances are mostly observed at high latitudes (Rino & Gonzalez, 1983) where phase scintillations are more prevalent than amplitude scintillations. On the contrary, at low latitudes, azimuthally oriented stripes are observed in SAR images that are predominantly formed due to the diffraction phenomenon causing amplitude scintillation (Belcher & Cannon, 2014). However, phase scintillation also occurs at low latitudes (Belcher et al., 2015). Apart from the scintillation strength, the structure and intensity of these stripes depend on the orientation of the ambient geomagnetic field and satellite along-track and scan directions at the location where the wave interacts with the irregularity structure (Meyer et al., 2016; Kim et al., 2017).

Studies involving ionospheric scintillations have utilized a variety of instruments, some of which include VHF and beacon receivers (Hunsucker, 1991), and the Global Positioning System (GPS; Ciraolo & Spalla, 1997; Rao et al., 2006). More recently, scintillation studies have been conducted using signals from global navigation satellite systems (GNSSs) other than GPS, including GLObal NAvigation Satellite System (GLONASS), Galileo, and Beidou (Morton et al., 2014). Electron density irregularities causing ionospheric scintillation affect these GNSS systems operating at L-band (1.57 and 1.22 GHz). The increasing popularity of GNSS and its integration with other systems makes the potential impact of scintillation on these systems ever more important. The development of the GNSS multifrequency systems aids not only in reducing the range errors but also in studying the scintillation phenomenon (Morton et al., 2014; Van de Kamp & Cannon, 2009). The signals' intensities and phases are processed to generate standard scintillation measurement indices, namely, amplitude scintillation (S_4; Whitney et al., 1969) and phase scintillation (σ_φ; Beniguel et al., 2009; Seif et al., 2011; Wernik et al., 2007), respectively. With knowledge of the satellite viewing geometry and receiver position, Rino (1979) and Rino and Fremouw (1977) derived the relationship between S_4 and the vertically integrated turbulence strength, C_kL (Secan et al., 1995).

Scintillation studies to date have been conducted predominantly using GPS satellite signals and other beacon satellite signals ranging in frequency from VHF through S-band. However, the sparse geographical spread of GPS stations over some regions of the globe is a major limitation in studying the scintillation phenomenon in these regions. Thus, it is desirable to consider data sets that have geographically a global and synoptic coverage. Since space-borne microwave SARs operating at L- and P-bands are also affected by ionospheric irregularities, they can provide a useful source of scintillation diagnostics. Recently, a number of authors (Belcher & Cannon, 2014; Belcher et al., 2017; Mannix et al., 2017) have been leveraging space-borne SAR signals for this purpose.

In this paper, the capability of polarimetric L-band SAR data is explored to quantitatively characterize the scintillation phenomenon in terms of scintillation measurement index, S_4, and vertically integrated turbulence strength, C_kL. This work includes data from satellites of the GLONASS and the GPS constellation. Henceforth, the term GNSS, in general, will be used throughout the text unless otherwise mentioned. C_kL and S_4 obtained from SAR and GNSS satellites are compared to show reasonable agreement between these different sources. The paper also compares these measurements for data sets on two dates in terms of varying total electron content (TEC), which can be an indicator of the scintillation strength. The comparison of geomagnetic activity indices also suggests the presence and absence of scintillations on the mentioned

days. Hence, for areas with no/less GNSS or ground-based data, SAR data can provide both qualitative and quantitative information about scintillation.

The details of the data set used and ionospheric conditions on the dates considered in the study are given in section 2. Following it, the measurement of scintillation parameters from GNSS stations and SAR are explained in sections 3 and 4, respectively, followed by a summary in section 5.

2. Data Sets Used

2.1. Fully Polarimetric SAR Data

The fully polarimetric SAR data used in the study were acquired from the Phased Array type L-band Synthetic Aperture Radar (PALSAR) on board Japan's Advanced Land Observation Satellite (ALOS-2). The acquisition was done in Full (HH, HV, VH, VV) pol high-sensitive mode (HBQ) with length of 70 km and width of 50 km in azimuth and range directions, respectively. The entire stretch of data was captured over the Indian subcontinent on two dates: 23 March 2015 (DoY 82, Orbit No. 04490) and 31 October 2016 (DoY 305, Orbit No. 13184). Both acquisitions took place during the ascending pass of the satellite orbit between 18:54 and 18:59 hr UT (LT = UT + 5 hr 30 min). As mentioned earlier, formation of ionospheric irregularities, in the equatorial region, occurs after local sunset. These irregularities develop relatively quickly (in 1–2 hr following local sunset) and then drift zonally as *fossilized* structures through the night as they decay. In the case of ALOS-2, the local sun times of the orbit are 12:00 ± 15 min in the descending node and 00:00 ± 15 min in the ascending node (http://www.eorc.jaxa.jp/ALOS-2/en/about/overview.htm). Although PALSAR-2 will fail to observe the peak of scintillation events, it succeeds to capture decaying irregularity structures at local midnight in its ascending pass.

A total of 26 scenes in each SAR orbit (52 scenes in total, see also supporting information) were processed for the study. The footprint of these scenes (Frames 0170–0420) stretches on the ground for a length of about 1,820 km. For a right-looking radar system in the ascending path, the scintillation effects are seen as stripes in the satellite along-track direction, oriented along the local geomagnetic field (**B**), as shown in Figure 1. The choice of the two periods has been made owing to the availability of the exact satellite orbits having the same look (off-nadir) angle.

The azimuthal streaking in SAR images due to amplitude scintillations have been widely reported by previous authors (Belcher & Cannon, 2014; Meyer et al., 2016; Shimada et al., 2008). As observed in the above data set, and also discussed in Meyer et al. (2016), the scintillations produce a characteristic striping pattern that is dependent on the local geomagnetic field orientation and the satellite orbital geometry. In the weak-scatter theory, the ionosphere is treated as a thin layer at a height of approximately 350 km (Rino, 1979), and we will follow this approach in our analysis. To comment on the morphology of stripes seen in the SAR data, the ambient geomagnetic field strength and direction at 350 km were calculated using the International Geomagnetic Reference Field-12 model (Thébault et al., 2015). As the satellite ascends in orbit near the southern tip of the Indian subcontinent, the stripes are less prominent in amplitude and widely separated (Figure 2a). Initially, the stripes are oriented with a clockwise rotation relative to the satellite track direction to the right aligned to the Earth's geomagnetic field. Upon further traveling northward, the stripes become more densely spaced within the same swath. In Figure 2b, the satellite orbit and magnetic field directions are nearly aligned, increasing the contrast of the stripe pattern. As the satellite leaves the anomaly region (Appleton, 1946), the stripes are oriented with a clockwise rotation relative to the satellite track. This is a consequence of the changing orientation of the geomagnetic field relative to the satellite direction of motion (Figure 2c).

To have a better visual comparison of the scintillation intensity affecting the SAR data on the 2 days, the Pauli RGB images of a scene (Frame 0320) acquired on both days are shown in Figure 3. In the Pauli RGB composite of a SAR image, the red represents double-bounce scattering (HH-VV), followed by green representing volume scattering (HV), and blue representing surface (HH + VV) scattering. Intensive streaking pattern in the direction of the local geomagnetic field can be seen for an image collected on 23 March 2015, which is a disturbed day (Figure 3a), while no such effect is seen in the second image acquired on 31 October 2016 that is a rather quiet day in terms of ionospheric scintillations (Figure 3b).
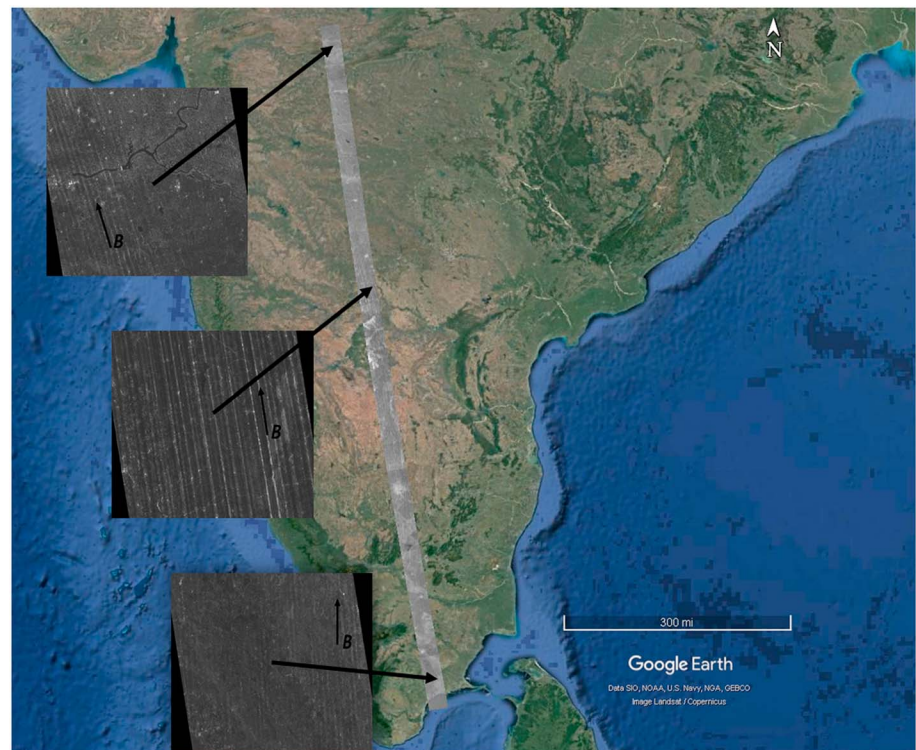
Figure 1. Phased Array type L-band Synthetic Aperture Radar-2 images acquired on 23 March 2015 over India. The footprint of the satellite track on ground is shown (black arrows point to the direction of the Earth's magnetic field calculated at a height of 350 km).

2.2. Planetary Geomagnetic Data

While scintillation activity and geomagnetic activity are not simply related (Basu et al., 2010), it is nevertheless useful to place the scintillation observations within the context of overall geomagnetic activity. The values of the sum of the three-hourly geomagnetic planetary index (K_p Sum) were 26+ and 16o for 23 March 2015 and 31 October 2016 dates, respectively. The maximum K_p value for the two dates were 4+ and 3o. Another
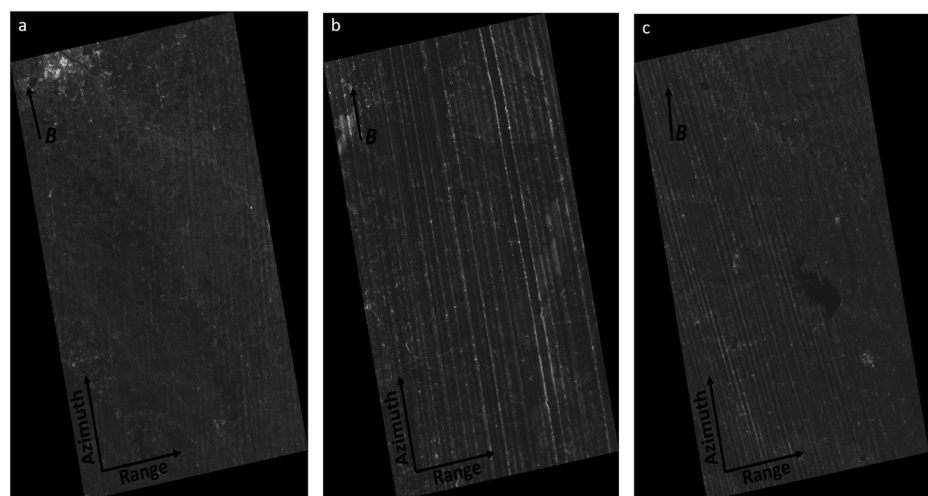
Figure 2. Images of three scenes (along with the scene ID and flight path) from the orbit path over the Indian subcontinent showing intensity, orientation, and spacing of ionospheric scintillations (black arrow shows the direction of Earth's magnetic field): (a) ALOS2044900180, (b) ALOS2044900280, and (c) ALOS2044900380.
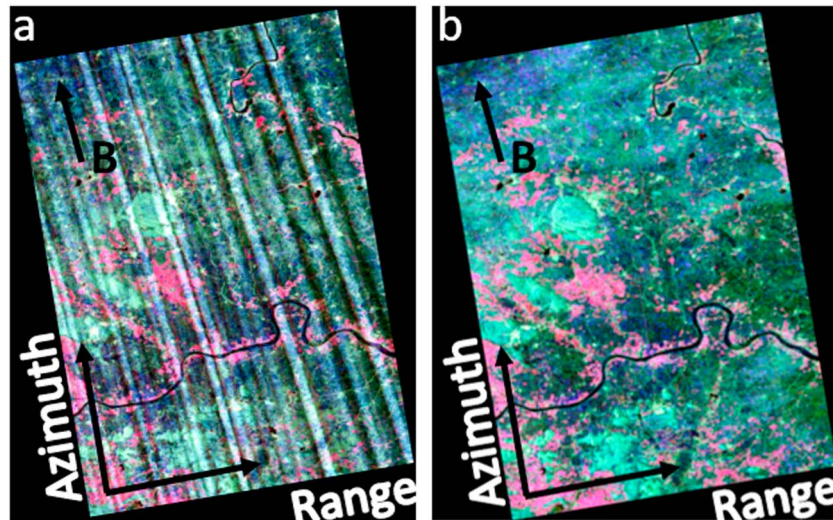
Figure 3. Comparison of Pauli RGB amplitude images showing data acquisition on (a) scintillation-affected day (23 March 2015) and (b) nonscintillation-affected day (31 October 2016).

comparison of daily A_p index (used interchangeably with K_p), 19 and 8 on the two dates, respectively, suggests that the geomagnetic conditions on the 2 days were slightly different. It should be noted that the data acquisition on 23 March was made only a few days after the powerful geomagnetic storm observed on St. Patrick's Day (17–18 March 2015; Astafyeva et al., 2015). Therefore, the moderately stronger geomagnetic activity on the 23rd might be expected. The subsequent section discussing the scintillation observations by GNSS satellites demonstrate that the first acquisition date, 23 March 2015, was an active scintillation night in comparison to the second day, 31 October 2016, which was an ionospheric quiet night with low/negligible scintillation activities. Since the GNSS and PALSAR systems both operate at L-band, both should experience similar levels of scintillation. Hence, through the paper we refer to the conditions on 23 March as disturbed with respect to the scintillation, while that on October 31 is referred to as quiet compared to the previous acquisition.

3. GNSS Satellites for Scintillation Observation

With a goal to establish a network of ground-based scintillation monitoring sensors worldwide, the Scintillation Network Decision Aid (SCINDA) collaborates with investigators hosting scintillation monitoring instruments in South America, Africa, and Asia (Carrano & Groves, 2006). For our area of study that typically covers the Indian Peninsula, S_4 data from two SCINDA GPS stations in India are utilized. These stations are located at Tirunelveli (TIR; geographic: 8.67°N, 77.81°E; geomagnetic: 0.17°N, 150.80°E), and Rajkot (RAJ; geographic: 22.30°N, 70.80°E; geomagnetic: 13.67°N, 151.94°E). The gap in latitudinal coverage from these two SCINDA GPS stations was completed by two TEC receivers at Mumbai (MUM; geographic: 19.013°N, 73.106°E; geomagnetic: 10.91°N, 147.16°E) and Nagpur (NAG; geographic: 21.15°N, 79.09°E; geomagnetic: 11.76°N, 152.02°E). These Septenrio PolaRxS receivers are installed by the Indian Institute of Geomagnetism, Navi Mumbai, in contrast to the NovAtel's GSV 4004B model receivers at SCINDA sites. All ionospheric measurements from GNSS receivers were computed over a 60-s time period.

3.1. Comparison of Vertical TEC and S_4 Index

Scintillation is an integrated effect of all irregularities encountered by the wave along the path of propagation. For the GNSS satellites, this propagation path is from the satellite to the receiver on the ground. In the case of SAR, the propagation path includes both the downward and upward transits of the wave through the ionosphere. The intensity of the irregularities that may be present is fundamentally limited by the density of the background plasma. Hence, measurements of TEC in the region help to place the scintillation measurements in proper context. The variance of electron density, that is, the absolute change in electron density fluctuations (ΔN) is proportional to the turbulence strength (Rino, 1979). Thus, TEC, essentially, places an
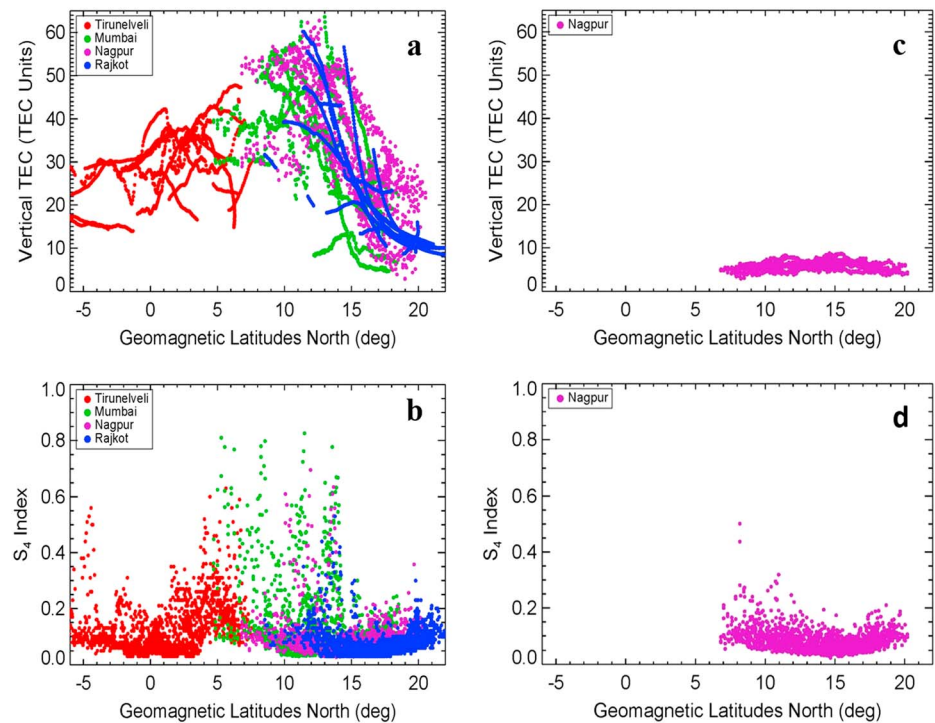
Figure 4. Vertical total electron content (TEC) and S_4 index plots from Global Positioning System satellites observed at four stations on 23 March 2015 (a, b) and 31 October 2016 (c, d), respectively.

upper bound on how large electron density fluctuations can be and hence on how strong scintillations can be at a particular frequency. For example, it is well known that scintillation tends to be strongest near the crests of the equatorial anomaly (Bhattacharya et al., 2014). This occurs because the high TEC regions have the potential to support intense irregularities with large variations in density. Of course, not all high TEC regions include irregularities, and so one must seek disturbances in the TEC for evidence that scintillation may occur. Evenings with very low TEC tend to be devoid of scintillations at L-band even if irregularities are present, because the variation in density within a low-density region is necessarily small (Bhattacharyya et al., 2003). In this section, we compare the TEC and scintillation observations from GNSS on the days of SAR acquisition.

TEC is the number of electrons measured along the ray path between the radio source and receiver and is measured in number of electrons per square meter, 1 TEC Unit (TECU) = 10^{16} electrons/m^2. GNSS receivers provide measures of differential pseudorange and differential carrier phase. These measurements are combined to produce a measure of relative slant TEC that must be calibrated to account for satellite and receiver interfrequency biases. We processed the data from all satellites in the GPS constellation observed at the four receiver stations of Rajkot, Tirunelveli, Mumbai, and Nagpur on 23 March 2015 and 31 October 2016. The TEC measurements were calibrated using the technique described in Carrano et al. (2009). Vertical TEC was computed by invoking the thin slab approximation to map the slant TEC measurements from the elevation angles to each satellite to the zenith.

Figure 4 shows the vertical TEC from all satellites in the GPS constellation observed at the four receiver stations of Rajkot, Tirunelveli, Mumbai, and Nagpur on 23 March 2015 and 31 October 2016. We note that we did not attempt to calibrate TEC data from the GLONASS constellation, which must be processed differently than the GPS TEC. In addition to TEC, the satellites also provided measurements of the amplitude scintillation index, S_4. Defined as the square root of the variance of normalized signal intensity, S_4 measures the amount of amplitude scintillation due to the disturbed ionosphere. The plots for vertical TEC and S_4 index versus geomagnetic latitude on both dates are also shown in Figure 4. Only data within a time window of 1900 UT ± 2 hr were included in these plots, intended to show the structure of the equatorial anomaly and scintillation activity near the time of the PALSAR pass.

On 23 March, the peak of TEC measurements, indicating the location of the northern crest of the equatorial anomaly, appears to be between 7° and 14°N geomagnetic latitude (Figure 4a), which is consistent with our expectation during this period of low solar activity. Disturbances in the TEC are manifested in the measurements from Tirunelveli, Mumbai, and Nagpur, while the TEC from Rajkot appears to be smoother by comparison. This is somewhat misleading, however, since a closer examination of the data revealed that Rajkot observed strong scintillations along satellite links to the south, and along those links, the TEC could not be measured due to repeated loss of lock. Presumably, the TEC along these links would have shown evidence of strong disturbances had the measurements been able to be made. The remaining TEC observations along undisturbed links in the west, east, and north directions were relatively smooth. The TEC tends to taper down after 15°N. Similar to the TEC plot, $S_4 > 0.3$ were observed above 2°N magnetic latitude with the strength of scintillation increasing after 6°N and continuing until 14°N (Figure 4b). As expected, the most intense scintillations were observed in the highest-density region near the crest of the equatorial anomaly.

It was unfortunate that the receivers at Rajkot, Mumbai, and Tirunelveli were down on 31 October, failing to record any data. Although a diurnal variation in TEC was observed at Nagpur on this date, apparently the values were rather small beyond 1600 UT. The data records at Nagpur within 1900 UT ± 2 hr show very low values of TEC (<10 TECU; Figure 4c). The S_4 measurements generally showed the lack of scintillation activity, except for a few samples with $S_4 > 0.2$ whose elevation angles were between 20° and 30° (Figure 4d). These few values of S_4 above the receiver noise floor were probably the result of multipath from terrestrial objects. The above comparative result of TEC and S_4 measures, along with the planetary geomagnetic indices, justifies our use of the terminologies *disturbed* and *quiet* days for 23 March 2015 and 31 October 2016, respectively. Since there was no ionospheric activity observed on 31 October, we have not included it in any of our following analysis of S_4 and C_kL from the GNSS satellites.

3.2. GNSS Measured S_4 Index and C_kL

The development of plasma bubble irregularities in the post-sunset *F* layer may be due to a number of contributing factors. The prereversal zonal electric field enhancement (PRE) which causes spread F is primarily due to the thermospheric eastward drift and the local gradients in the Pedersen conductivity formed across the sunset terminator (Abdu et al., 2006; Rishbeth, 1971). Because of the eastward drift, the ionospheric irregularities causing amplitude scintillations in SAR could have been observed by GNSS satellites both prior to and post-observation by SAR. More precisely stated, knowledge of the zonal irregularity drift may be used to compare the GNSS and SAR observations at a time when both systems would have been expected to observe irregularities along the same magnetic meridian. Due to the increased mobility of electrons along magnetic field lines, ionospheric irregularities are highly correlated along magnetic meridians. Thus, even though the GNSS and SAR signals are observing different volumes of disturbed plasma and at different times, it is possible to make a meaningful comparison of the scintillations observed by these two systems by accounting for the zonal irregularity drift. Additional details on how we compared the GNSS and SAR observations of S_4 and C_kL are given later in this section.

Spaced receivers cross-correlating GPS signals for drift velocity measurement are a proven technique (Spatz et al., 1988; Vacchione et al., 1987). However, in the absence of a sufficiently closely spaced pair of receivers in the region, the zonal irregularity drift was estimated using the phase scintillation index (σ_φ) and amplitude scintillation index (S_4) from GNSS measurements at a single station (Carrano et al., 2016). This method uses the $(\frac{\sigma_\varphi^2}{S_4^2})$ ratio along with knowledge of the propagation and scan geometries, and phase spectral index (p) to infer the effective scan velocity. The effective scan velocity is a measure of the relative velocity between the satellite scan and drifting irregularities at the ionospheric pierce point (IPP) height but also accounts for the anisotropy of the field-aligned irregularities. The irregularity zonal drift was derived from the effective scan velocity assuming that at low latitudes, this drift is purely eastward (neglecting northward and vertical components). The zonal irregularity drift, shown in Figure 5b, from GNSS satellites (bearing pseudo random noise identifiers (PRNs) 12 and 20) viewed at Tirunelveli (TIR), was calculated to be 80–130 m/s, averaged about ~100 m/s. The linear relationship between S_4 and σ_φ, used in computing the scan velocity, is shown in Figure 5a.

Keeping this in mind, in our subsequent analysis, we have included scintillation data from all GNSS satellites for which an irregularity at the ionospheric penetration point would have to travel eastward between 50 and
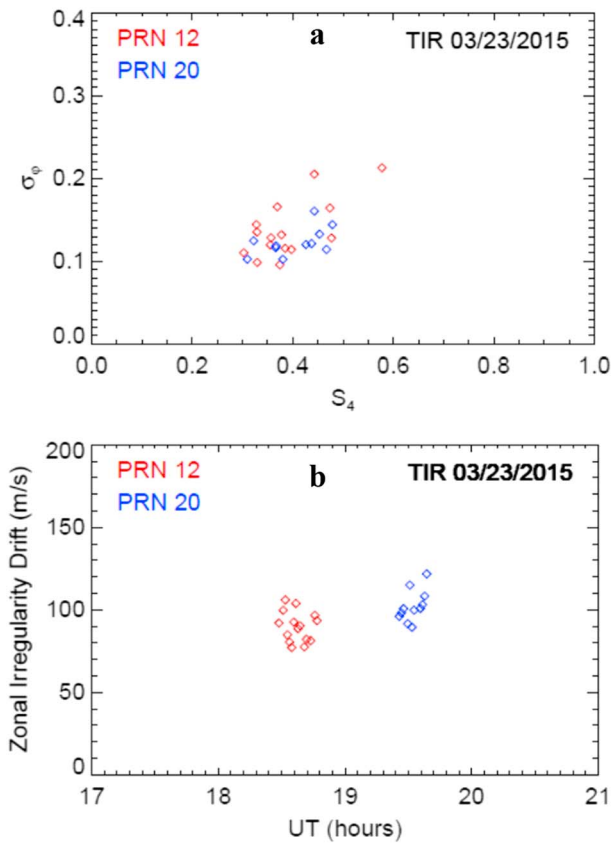
Figure 5. (a) σ_φ versus S_4 and (b) zonal irregularity drift versus measured at Tirunelveli (TIR) on 23 March 2015. PRN = pseudo random noise identifier.

150 m/s in order to reach the ALOS-2 at ~1900 UT. We used the range 50–150 m/s to account for some uncertainty in our estimate of the zonal drift. The position of satellites and SAR were calculated at a common reference IPP height of 300 km. GNSS satellites to the east of SAR track, satisfying the velocity criterion, were also included as they may have observed the irregularity after ALOS-2 pass. Figure 6 shows the footprints of all GNSS satellites included along with the SAR track at IPP. Satellites labeled with PRNs between 1 and 31 belong to the GPS constellation. Those labeled with PRNs between 38 and 61 correspond to GLONASS slot numbers with an offset of 37. It is expected that GNSS satellites to the west of SAR track observed the irregularity at a time earlier to the SAR pass. The drifting patch was then captured by SAR during its pass over the region, followed by a few more GNSS satellites on the east post at ~1900 UT.

Shown in Figure 7 are the S_4 plots for those GNSS satellites whose data satisfy the velocity constraint and also observed scintillation within 90 min of the SAR collected on 23 March 2015. The time window corresponding to the irregularity drift range of 50–150 m/s for each satellite is highlighted on their plots with a light-blue band. The S_4 measurements were collected from satellites at sufficiently high elevation angles (>20°) such that multipath reflections from terrestrial features can be expected to be negligible.

All observable GNSS satellites that may have captured that night's strong scintillation activity, during the time highlighted by the blue band, for Tirunelveli and Rajkot stations have an average one-way S_4 of 0.17 and 0.7, respectively. The satellites, observed at Mumbai, whose IPPs correspond to the central portion of SAR pass (PRNs 5, 51, and 52) have an average of 0.53 while those located further up north (PRNs 24 and 53) have a comparatively lower average S_4 of 0.18. The trend from these values is, thus, an indicator of a strong scintillation whose peak was observed between 13°and 19° geographic north latitude. No data from Nagpur satisfied the velocity criteria and, therefore, are not included in the comparative study.

S_4 is a direct measure of the scintillation phenomenon and is dependent on the geometry with which the signal intercepts the signal, as well as the frequency of the signal and the characteristics of the random ionospheric medium. The propagation geometry is different for each GNSS satellite, even though they are all
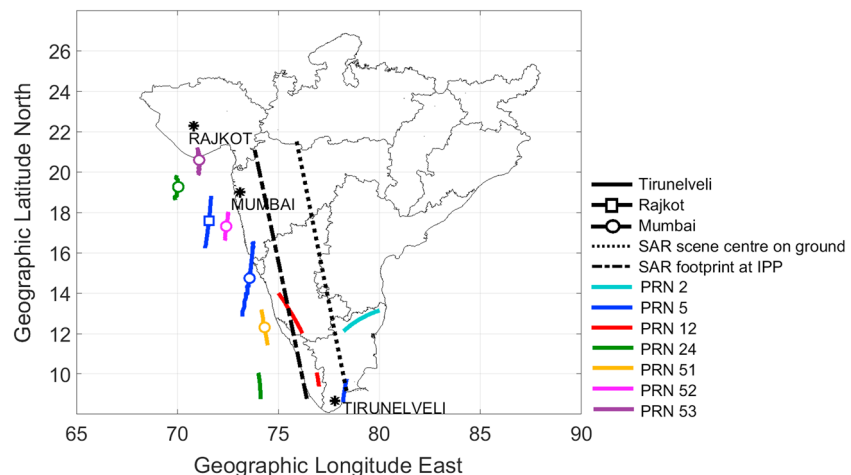
Figure 6. Footprints of the global navigation satellite system and Phased Array type L-band Synthetic Aperture Radar tracks at ionospheric pierce point (IPP) height of 300 km. PRN = pseudo random noise identifier.
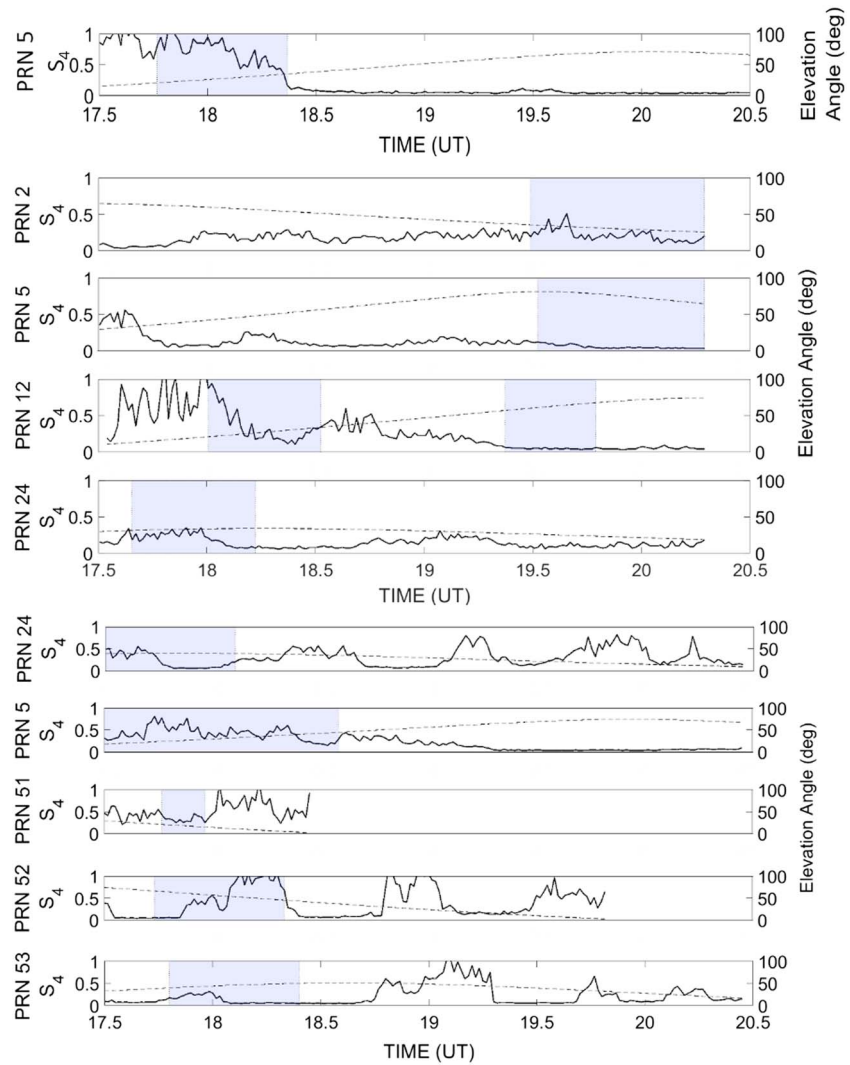
Figure 7. S_4 index and elevation angle plot for global navigation satellite system satellites at (a) Rajkot, (b) Tirunelveli, and (c) Mumbai. PRN = pseudo random noise identifier.

viewed from the same station. In order to remove the effects of the propagation geometry, it is often desirable to describe the scintillation conditions in terms of C_kL. Defined as the vertically integrated turbulence strength, C_kL is exclusively a property of the ionospheric medium.

Using the thin layer Born approximation for one-way propagation, from Rino and Fremouw (1977) and Rino (1979), one-way S_4 can be converted to C_kL by inverting the expression

$$S_4{}^2 = r_e{}^2 \lambda^2 C_k L \sec\theta \left(\frac{2\pi}{1,000}\right)^{2v+1} \left(\frac{\lambda z_r}{4\pi}\right)^{v-\frac{1}{2}} \frac{\Gamma\left[\frac{2.5-v}{2}\right]}{2\sqrt{\pi}[(v+0.5)/2](v-0.5)} \mathscr{J} \tag{1}$$

In the above, r_e is the classical electron radius, λ is the signal wavelength, z_r is the reduced propagation distance between the target and ionospheric layer after correcting for the spherical wavefront, Γ is the Gamma function, θ is the propagation angle, $\mathscr{J}$ is the geometry factor, and v is the spectral index ($p = 2v$, where p is the phase spectral index). Details for calculating z_r and $\mathscr{J}$ are given in Rino (1979).

The above conversion was performed for all the GNSS satellites observed at the Tirunelveli, Rajkot, and Mumbai stations to calculate the C_kL, assuming an IPP height of 300 km. We note that the spectral index, p, was not derived from the data since high rate phase measurements were not available from these

stations. Hence, we assumed a value of $p = 2.5$, which is used in the WideBand Scintillation Model (Secan et al., 1995). To compute the geometry factor J, one must also assume a value for the anisotropy of the irregularities. We have assumed a 50:1 ratio between the correlation length of the irregularities along and across the magnetic field direction. This choice is not critical, since the relationship between S_4 and $C_k L$ becomes insensitive to this ratio once it exceeds 10:1 (Rino, 1979). It is evident that $C_k L$ computed at Rajkot are larger than at Tirunelveli stations with average $C_k L$ being 2.29×10^{34} and 2.14×10^{33}, respectively. The $C_k L$ calculated for Mumbai station showed the same trend as S_4 with $C_k L$ of 1.91×10^{34} and 5.5×10^{33} at the center and toward the northern end of the SAR track. These values are independent of the viewing geometry and thus a better estimate of the turbulence strength associated with the disturbed ionosphere.

Although the GNSS receivers are able to measure S_4 and $C_k L$ values, their reach is restricted to a relatively small geographic area. In this regard, the use of another signal source, similarly affected by scintillations but providing a wider swath, is quite useful. Thus, the use of SAR satellites operating at L- and P-bands would make a valuable contribution to ionospheric studies. For example, with SAR, it is possible to characterize scintillation activity and irregularities in the equatorial anomaly structure over landmass regions. Multiple GNSS receivers are required to accomplish the same in any given longitude sector.

4. SAR for Scintillation Studies

Multitemporal SAR data over a common area helps us draw conclusions about the surface from the backscatter. When SAR sensors are affected by scintillation, the information contained in the backscattered signal is altered. It now includes information pertaining to the ionospheric irregularities as well as the terrain. Assuming that the ground has not changed over the time span of two acquisitions, the radar backscatter can be exploited to isolate the contribution from the ionosphere.

Previous works by Belcher and Cannon (2014), Mannix et al. (2017), and Belcher et al. (2017) have demonstrated the capability of measuring S_4 and $C_k L$ using SAR signals. SAR data acquired under different ionospheric conditions may also have varying background returns due to changes in the terrain over time. However, assuming the condition of background homogeneity with no change in the terrain, S_4 and $C_k L$ can be calculated from a pair of images of the same geographic region provided that one of the images is unaffected by scintillation.

4.1. S_4 From Image Contrast Method

In the paper of Belcher and Cannon (2014), the authors have identified the possibility of determining S_4 from a pair of SAR images using the so-called contrast method. This method assumes that the stochastic sum of amplitude samples over a Fresnel zone determines the effects of amplitude scintillation on SAR. In addition, since the length of the synthetic aperture is longer than the Fresnel zone, the gamma-distributed SAR amplitude will be integrated over N such independent Fresnel zones (Belcher & Cannon, 2014). The contrast C_d, the standard deviation divided by the mean of the ratio between disturbed- and quiet-day images, from a pair of SAR images at HH polarization, is used in our work. It can be related to the one-way amplitude scintillation index, S_4, as

$$S_4^2 = \frac{N}{12}\left(C_d^2 - 4 + 4\sqrt{1 + C_d^2 + \frac{C_d^4}{16}}\right) \qquad (2)$$

where $N = \frac{L_{SA}}{\gamma Z_F}$ is the number of independent amplitude scintillation samples, L_{SA} is the length of synthetic aperture, γ is the ratio between the spatial distance along the aperture and the effective distance along the phase screen, and Z_F is the size of the Fresnel zone. The limiting factor in this equation is N. Hence, the choice of spectral index and anisotropy ratio serves as important inputs to the model. As in the case of our earlier analysis of the GNSS data, a phase spectral index of 2.5 and an anisotropy ratio of 50:1 was assumed when computing γ at the phase screen height. The assumption of 50:1 axial ratio is supported by our further investigation on the sensitivity of the axial ratio to the calculation of number of independent Fresnel zones N. We have inferred that beyond the value of 30:1, N is insensitive to changes in the axial ratio for the SAR data under consideration. This assumption is also supported by the WBMOD at low latitudes (Secan et al., 1995).
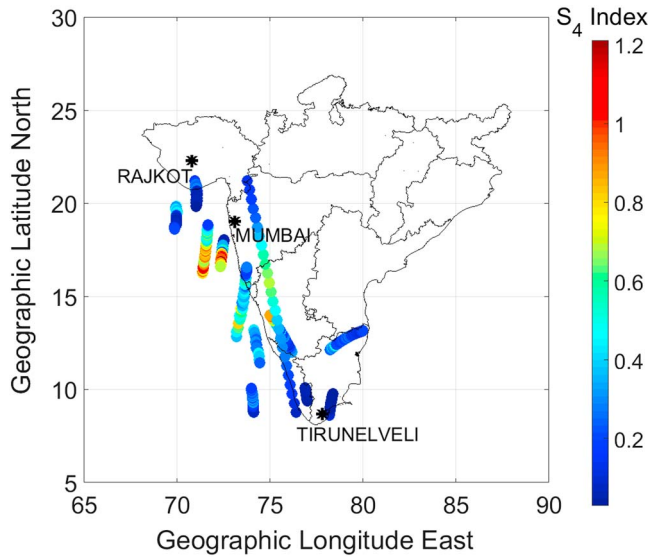
Figure 8. S_4 index plot for the global navigation satellite system and synthetic aperture radar at ionospheric pierce point (IPP) height of 300 km.

4.2. S_4 From Enhancement in Radar Cross Section

An alternative method to calculate S_4 from SAR images is using the increase in the two-way backscatter intensity that occurs when imaging the ground in the presence of scintillation. As highlighted in Knepp and Houpis (1991), the additional ray paths illuminate a target, apart from the direct beam, because of scatter from the irregularity layer during the occurrence of scintillation. This multiple interference increases the mean of the two-way backscatter intensity. Observed mostly in monostatic radars and to some extent in small bistatic angle systems (Belcher & Cannon, 2014), the ratio of the mean radar cross section (RCS) from SAR image pairs, with and without scintillation effects, can be related to two-way S_4 as

$$\mu_2 = \mu^2\left(1 + S_4^2\right) \tag{3}$$

where μ and μ_2 are the mean RCS measured from SAR images acquired under undisturbed and disturbed ionospheric conditions. The so-called RCS enhancement method depends on the selection of a common region of interest in the image pair. Under the assumption of a constant RCS in the undisturbed image, increased and decreased RCS is observed in the disturbed image.

Both methods of estimating S_4 from SAR can serve as complimentary checks to our calculation. However, each comes with its pros and cons. Although we assume constant RCS in the undisturbed image, in reality the backscatter changes rapidly over time, even when homogeneous background conditions are assumed. The contrast method heavily relies upon the assumption of statistically invariant ionosphere and the correct estimate of N. Therefore, in the absence of accurate measurements for the anisotropy ratio and spectral index of irregularities, a degree of uncertainty is associated with this method also.

4.3. S_4 Measurements From SAR

In this paper, the S_4 was calculated using both the contrast method and backscatter enhancement method. Before calculating S_4, the two SAR images were first calibrated (Motohka et al., 2018) followed by coregistration using the image-to-image cross-correlation technique. A cubic convolution interpolation with the RMS threshold of 0.05 pixels was chosen. The loss in contrast calculation followed by the average S_4 calculation was performed using the method adopted by Mannix (2016). As most of the images were completely affected by amplitude scintillations, the RCS enhancement method was applied to the entire image, to avoid any bias in selection of regions of interest. Similar to the contrast technique, the choice of the size of subimages is adopted as explained in Mannix (2016), where subgrouping is done in both range and azimuth. The average two-way S_4 computed from the RCS enhancement method, for each subimage, was converted into one-way S_4 using

$$S_{4\times2}^2 = 4S_4^2 + 2\frac{S_4^4}{S_4^2 + 1} \tag{4}$$

where S_4 and $S_{4\times2}$ are the one-way and two-way S_4, respectively. Equation (4) was derived by Knepp and Houpis (1991) assuming that the normalized intensity variations are distributed with Nakagami-m statistics. Though the study includes results from HH-polarized SAR data for the computation of S_4, we have calculated S_4 at HV, VH, and VV to find that ionospheric irregularities cause the same propagation effects at other polarizations.

The one-way S_4 measured from all GNSS satellites at the three receiver stations, satisfying the velocity constraint, along with those measured from SAR, using the RCS method, are plotted in Figure 8. These values are plotted at the IPP height of 300 km used for calculation. The positions of the GNSS satellites can be identified with reference to Figure 6. The peak S_4 region computed from SAR corresponds to the 13.5–18.2° north geographic latitude, with the maximum value being 0.63. This latitude range corresponds to the SAR scenes (Frames 260–350) where the streaks are most evident (refer to Figures 2b and 3a). The stretch of strong
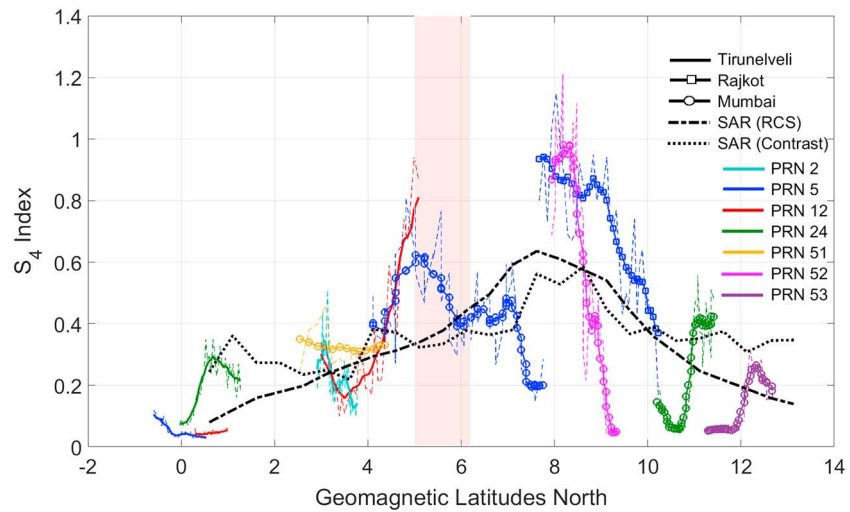
Figure 9. S_4 index versus geomagnetic latitude from the global navigation satellite system and synthetic aperture radar. PRN = pseudo random noise identifier.

scintillation is consistent with the large S_4 measurements from GNSS satellites between 13° and 19°N. Furthermore, the geographic extent approximately covers the range of geomagnetic latitudes at which the GPS TEC is largest, namely, the northern crest of the equatorial anomaly.

To facilitate a better visual comparison of the scintillation measurements from SAR and GNSS and their relation to the equatorial anomaly (refer to Figure 4), the S_4 data are replotted as a function of geomagnetic latitude in Figure 9. Here S_4 values from SAR computed using the contrast and backscatter enhancement methods are shown along with the GNSS measurements. The S_4 values measured by GNSS with 1-min resolution are more highly variable than the SAR estimates, which are effectively derived from spatial and temporal averages of the data. In an effort to bring the measurements from SAR and GNSS onto a common spatial scale, the S_4 from GNSS are averaged using an 11-min moving window. This window size is selected using the following reasoning. In the stripmap mode, a particular PALSAR-2 scene of 70 km in the azimuth is acquired in 8 s. The data in each such scene have been spatially averaged to compute the S_4. Since the PALSAR scans through the ionosphere so quickly, the data provide what is essentially an instantaneous snapshot of the irregularities. The GNSS satellites are farther away and move much more slowly, such that the line of sight scans through the irregularities at roughly 100 m/s. It would hence take approximately 700 s (~11 min) to scan through 70 km of ionospheric structure (the distance scanned by the SAR to produce each S_4 estimate). The broken lines for GNSS satellites in Figure 9 show the data at 1-min intervals, with the 11-min temporally averaged data overlaid with the solid lines.

One can expect accurate SAR estimates of S_4 only to the extent to which the assumptions required for each technique are valid. When applying the contrast method, the terrain must be statistically homogenous and unchanged in the disturbed and undisturbed images. When applying the RCS enhancement method, the radar backscatter from the ground must be unchanged in the disturbed and undisturbed images. Both techniques invoke the weak scatter theory to describe the effects of scintillation and thus may not provide accurate results when S_4 exceeds about 0.6. Discrepancies between S_4 estimates produced using the two techniques may suggest that conditions required for one or both methods are being violated. That being said, we found the estimates using the contrast and RCS enhancement methods to generally be in good agreement. The small red patch highlighted in the above figure corresponds to the two SAR scenes (Frames 0280 and 0290), which are acquired over what visually occurs to be a statistically homogeneous terrain. It is thus encouraging that the S_4 values calculated from both methods have nearly equal values in this region. The largest discrepancy between the SAR S_4 values obtained from the two methods occurs when the scintillation is weak (within the range 0–2° and 11–14° geomagnetic latitude). We might conjecture that the RCS enhancement method may be less sensitive to low levels of scintillation, whereas the contrast method is responsive to irregularities that are too weak to produce an RCS enhancement and visual streaks in the
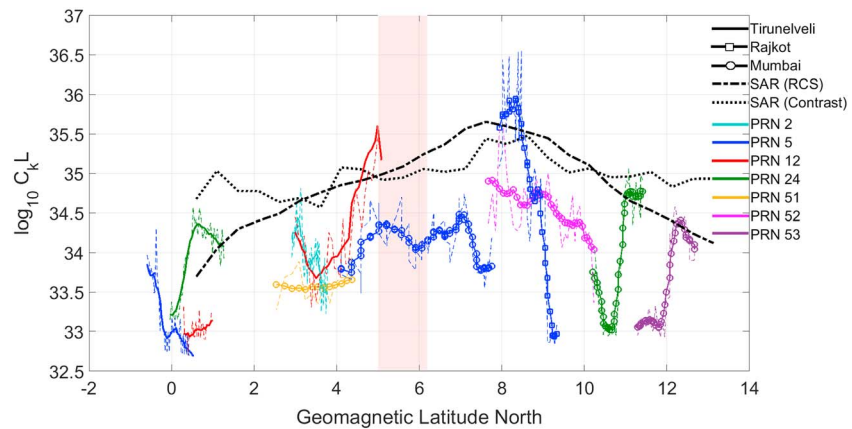
Figure 10. $\log_{10}C_kL$ versus geomagnetic latitude from the global navigation satellite system and synthetic aperture radar. PRN = pseudo random noise identifier.

image. This possibility was, in fact, conjectured by previous authors (Belcher et al., 2017), but one would need to consider a wider collection of data to establish whether this is the case.

The agreement between the SAR estimates of S_4 and those measured directly with GNSS is also very encouraging. Both the SAR and GNSS S_4 values show elevated scintillation intensity near the northern crest of the anomaly as indicated by the GNSS TEC (Figure 4). The scintillation intensity is lowest near the dip equator and northward of the crest where the TEC is lower. The GNSS S_4 measurements show more variability than the SAR measurements, which is not surprising since the GNSS satellites are scanning through the irregularities and viewing them along very different viewing geometries. While an effort has been made to compare the SAR measurements with only those GNSS measurements, which could have reasonably sampled the same irregularities at an earlier or later time as the SAR, it is very difficult to make common volume measurements with the two systems. Overall, however, we consider the agreement between the SAR and GNSS measurements of S_4 to be quite good.

4.4. C_kL Measurements From SAR

Previous authors (Belcher et al., 2017; Mannix et al., 2017) have estimated C_kL from SAR measurements, using point targets and ground clutter statistics, respectively. In the absence of corner reflectors serving as point targets and accurate backscatter statistics due to inhomogeneous terrains, the knowledge of satellite position and viewing geometry were used to convert the S_4 measured by the contrast or RCS enhancement methods to C_kL along with assumed values of anisotropy ratio of 50:1 and phase spectral index of $p = 2.5$. The C_kL values computed from GNSS and SAR data assuming an IPP altitude of 300 km are plotted in Figure 10. Removing the effect of viewing geometry, the C_kL computed from GNSS satellites generally reduces the spread between the curves corresponding to different satellites. This supports the notion that all these satellites saw the same patch and/or patches of irregularity during that evening. As can be observed in Figures 9 and 10, there is a discontinuity in the calculation of S_4 and C_kL, respectively, for PRN 5 near 7–8° north magnetic latitudes. The reason for this discontinuity is that even when Mumbai and Rajkot are viewing the same satellite (PRN 5), the ionospheric penetration points to this satellite differ substantially in longitude when viewed from two stations. Since this longitude difference also implies a difference in solar local time, the two stations are in fact observing different irregularities at different stages of their evolution even when they are viewing the same satellite. Figure 6 shows this clearly. The IPP of PRN 5 is several degrees (2.5°) more westward for Rajkot compared to Mumbai. It would take the bubble traveling at 100 m/s about 2.5 hr to traverse 2.5° of longitude, during which time the bubble has been decaying. Rajkot sees the irregularities at an earlier stage of their evolution while they are stronger (having larger C_kL), while Mumbai sees them later in the evening while they are decaying (smaller C_kL).

We observe from Figure 10 that C_kL values estimated from SAR follow the same trend as the GNSS estimated values but tend to overestimate the GNSS results. While it is not obvious why this should be the case, we note

that the mapping from S_4 to C_kL is known to be more reliable for higher elevation satellite passes (Cervera & Thomas, 2006). Many of the GNSS observations were acquired at relatively low elevation angles (which could lead to inaccurate C_kL estimates), whereas the SAR data were collected at >59° elevation and parallel side-looking data acquisition. The viewing geometry from PRN 24 to Mumbai and Tirunelveli, conversely, has a viewing geometry that is nearly parallel to the viewing geometry of the SAR, and the estimates of C_kL from this GNSS satellite agree with the SAR estimate reasonably well. As with the S_4 plot (Figure 9), the C_kL values computed per minute at each IPP position of the GNSS satellite are shown with broken-colored lines. The 11-min averaged data, conversely, are overlaid with solid lines. The portion of the plot highlighted by the light-red stripe relates to the two SAR scenes assumed to have uniform background. As with S_4 values, the C_kL estimates made using the contrast method and RCS enhancement method are quite similar in this region.

5. Conclusion

GNSS satellite signals are widely used for scintillation studies. However, the relative sparsity of receiver stations in certain regions on the globe inspires us to explore the capabilities of other systems to complement such studies. In this paper, the authors have used low-frequency SAR data for ionospheric scintillation studies. A long stretch of ALOS-2/PALSAR-2 acquisitions over the Indian subcontinent on two dates of varying ionospheric scintillation conditions facilitates this study, which allows us to characterize scintillation activity throughout the equatorial anomaly region over land using a single instrument.

GPS data from two Indian stations in the SCINDA network and two TEC receivers have been used to measure the TEC, and S_4 index demonstrate the varied ionospheric conditions of the two dates included in our study. High values of TEC coupled with higher S_4 index values implied strong signal scattering and scintillation on 23 March 2015. Although data from the majority of the stations were not collected on 31 October 2016, the extremely low values of TEC and S_4 from Nagpur station indicates negligible scintillation activity on that day. The amplitude scintillation S_4 index and the viewing geometry were used to estimate the strength of turbulence C_kL from both the GNSS and SAR data. The comparison in terms of C_kL is helpful in that the turbulence strength is a property of the random ionospheric medium and independent of viewing geometry. The C_kL values are indicative of the increased ionospheric irregularity strength leading to scintillation.

Pairs of SAR scenes over the same terrain have been utilized to calculate S_4 indices by two previously published techniques, image contrast and radar backscatter enhancement. These S_4 measurements are compared with each other and with direct observations of S_4 from GNSS. All three measurements show a similar trend that shows an enhancement at 6–9.5°N magnetic latitudes near the northern equatorial anomaly crest, as identified using GNSS TEC. While the exact measure of anisotropy ratio and spectral index limits the accuracy of the contrast method, the assumption of a constant radar backscatter in an undisturbed image is the limiting drawback of the RCS technique. Despite these shortcomings, an attempt has been made to compute S_4 for the SAR pairs. Entire scenes, with swaths of 70×50 km in azimuth and range, have been spatially averaged to compute S_4. The temporal equivalent of this averaging has been included in GPS measurements by averaging over an appropriate moving window.

With the help of information about the GNSS satellites' viewing geometry with respect to the receiver, the S_4 has been converted into C_kL and compared with the corresponding values obtained from SAR. For SAR scenes, C_kL have been calculated assuming the central position of the platform, at the flying altitude, as the transmitter location and the scene center location on ground as the receiver position. This assumption may have averaged out small fluctuations within the SAR scene. While the PALSAR-2 observations of C_kL tended to be larger compared to those inferred from GNSS, a reasonable degree of correlation between the two sources goes on to demonstrate that SAR data complements GNSS in scintillation studies. We note that a constant value of phase spectral index ($p = 2.5$) was assumed for the calculations in this study, since we did not attempt to infer it from the scintillation data itself. It is possible that the agreement between the CkL values from SAR and GNSS would improve if the value of p were measured and used in the calculations, but we did not verify this.

The manifestation of scintillation on SAR images also provides insights into their geophysical characteristics. Origin, growth, and strength of ionospheric irregularities causing scintillation can be identified from their varied effects on SAR, such as the azimuth stripes caused by amplitude scintillations. This paper, for example,

offers the potential of SAR in quantifying the strength of observed ionospheric scintillations in regions with sparse GNSS networks. It also highlights the capability of SAR in capturing wider coverage of the phenomenon compared to point measurements from GNSS receivers. The wealth of data acquired in the past by both L-band SARs, ALOS-1 and ALOS-2, and to be acquired in the future by ALOS-2, can be harnessed to further investigate the dynamics of the ionosphere.

References

Abdu, M., Iyer, K., de Medeiros, R., Batista, I., & Sobral, J. (2006). Thermospheric meridional wind control of equatorial spread F and evening prereversal electric field. *Geophysical Research Letters*, *33*, L07106. https://doi.org/10.1029/2005GL024835

Alizadeh, M. M., Wijaya, D. D., Hobiger, T., Weber, R., & Schuh, H. (2013). Ionospheric effects on microwave signals. In J. Böhm, & H. Schuh (Eds.), *Atmospheric effects in Space Geodesy* (pp. 35–71). Berlin: Springer Atmospheric Sciences, Springer. https://doi.org/10.1007/978-3-642-36932-2_2

Appleton, E. (1946). Two anomalies in the ionosphere. *Nature*, *157*(3995), 691–691. https://doi.org/10.1038/157691a0

Astafyeva, E., Zakharenkova, I., & Forster, M. (2015). Ionospheric response to the 2015 St. Patrick's Day storm: A global multi-instrumental overview. *Journal of Geophysical Research: Space Physics*, *120*, 9023–9037. https://doi.org/10.1002/2015JA021629

Basu, S., Basu, S., MacKenzie, C., Bridgwood, C., Valladares, C., Groves, K., & Carrano, C. (2010). Specification of the occurrence of equatorial ionospheric scintillations during the main phase of large magnetic storms within solar cycle 23. *Radio Science*, *45*, RS5009. https://doi.org/10.1029/2009RS004343

Belcher, D. (2008). Theoretical limits on SAR imposed by the ionosphere. *IET Radar, Sonar and Navigation*, *2*(6), 435–448. https://doi.org/10.1049/iet-rsn:20070188

Belcher, D., & Cannon, P. (2014). Amplitude scintillation effects on SAR. *IET Radar, Sonar and Navigation*, *8*(6), 658–666. https://doi.org/10.1049/iet-rsn.2013.0168

Belcher, D., Cannon, P., & Gustavsson, A. (2015). The ascension island experiment: Measurement of ionospheric scintillation effects on PALSAR-2. IEEE International Geoscience and Remote Sensing Symposium (pp. 3191–3194). Milan, Italy, IEEE.

Belcher, D., Mannix, C., & Cannon, P. (2017). Measurement of the ionospheric scintillation parameter CkL from SAR images of clutter. *IEEE Transactions on Geoscience and Remote Sensing*, *55*(10), 5937–5943. https://doi.org/10.1109/TGRS.2017.2717081

Belcher, D., & Rogers, N. (2008). Theory and simulation of ionospheric effects on synthetic aperture radar. *IET Radar, Sonar and Navigation*, *3*(5), 541–551. https://doi.org/10.1049/iet-rsn.2008.0205

Beniguel, Y., Romano, V., Alfonsi, L., Aquino, M., Bourdillon, A., Cannon, P., et al. (2009). Ionospheric scintillation monitoring and modelling. *Annals of Geophysics*, 391–416. https://doi.org/10.4401/ag-4595

Bhattacharya, A., Kakad, B., Sripathi, S., Jeeva, K., & Nair, K. (2014). Development of intermediate scale structure near the peak of the *F* region within an equatorial plasma bubble. *Journal of Geophysical Research: Space Physics*, *119*, 3066–3076. https://doi.org/10.1002/2013JA019619

Bhattacharyya, A., Groves, K. M., Basu, S., Kuenzler, H., Valladares, C. E., & Sheehan, R. (2003). L-band scintillation activity and space-time structure of low latitude UHF scintillations. *Radio Science*, *38*(1), 1004. https://doi.org/10.1029/2002RS002711

Briggs, B. H. (1975). Ionospheric irregularities and radio scintillations. *Contemporary Physics*, *16*(5), 469–488. https://doi.org/10.1080/00107517508210825

Carrano, C., Anghel, A., Quinn, R., & Groves, K. (2009). Kalman filter estimation of plasmaspheric total electron content using GPS. *Radio Science*, *44*, RS0A10. https://doi.org/10.1029/2008RS004070

Carrano, C., & Groves, K. (2006). The GPS segment of the AFRL-SCINDA global network and the challenges of real-time TEC estimation in the equatorial ionosphere. Proceedings of the 2006 National Technical Meeting of the Institute of Navigation, (pp. 1036-1047). Monterey, CA.

Carrano, C., Groves, K., & Caton, R. (2012). Simulating the impacts of ionospheric scintillation on L band SAR image formation. *Radio Science*, *44*, RS0L20. https://doi.org/10.1029/2011RS004956

Carrano, C., Groves, K., Rino, C., & Doherty, P. (2016). A technique for inferring zonal irregularity drift from single-station GNSS measurements of intensity (S_4) and phase (σ_φ). *Radio Science*, *51*, 1263–1277. https://doi.org/10.1002/2015RS005864

Carter, B. A., Tulasi Ram, S., Yizengaw, E., Pradipta, R., Retterer, J., Norman, R., et al. (2018). Unseasonal development of post-sunset *F*-region irregularities over Southeast Asia on 28 July 2014: 1. Forcing from above? *Progress in Earth and Planetary Science*, *5*(1), 1–12. https://doi.org/10.1186/s40645-018-0164-y

Cervera, M., & Thomas, R. (2006). Latitudinal and temporal variation of equatorial ionospheric irregularities determined from GPS scintillation observations. *Annales Geophysicae*, *24*(12), 3329–3341. https://doi.org/10.5194/angeo-24-3329-2006

Ciraolo, L., & Spalla, P. (1997). Comparison of ionospheric total electron content from the Navy Navigation Satellite System and the GPS. *Radio Science*, *32*(3), 1071–1080. https://doi.org/10.1029/97RS00425

Hunsucker, R. (1991). Satellite, rocket, and other techniques. In R. Hunsucker (Ed.), *Radio techniques for probing the terrestrial ionosphere*, (pp. 185–228). Berlin, Heidelberg: Springer. https://doi.org/10.1007/978-3-642-76257-4, ISBN: 978-3-642-76257-4

Hysell, D. L., Fritts, D. C., Laughman, B., & Chau, J. L. (2017). Gravity wave-induced ionospheric irregularities in the postsunset equatorial valley region. *Journal of Geophysical Research: Space Physics*, *122*, 11,579–11,590. https://doi.org/10.1002/2017JA024514

Ishimaru, A., Kuga, Y., Liu, J., Kim, Y., & Freeman, A. (1999). Ionospheric effects on synthetic aperture radar at 100 MHz to 2 GHz. *Radio Science*, *34*(1), 257–268. https://doi.org/10.1029/1998RS900021

Jin, Y., Moen, I., Oksavik, K., Spicher, A., Clausen, L. B., & Miloch, W. J. (2017). GPS scintillations associated with cusp dynamics and polar cap. *Journal of Space Weather and Space Climate*, *7*, 1–12. https://doi.org/10.1051/swsc/2017022

Kim, J. S., Papathanassiou, K., Sato, H., & Quegan, S. (2017). Detection and estimation of equatorial spread F scintillations using synthetic aperture radar. *IEEE Transactions on Geoscience and Remote Sensing*, *55*(12), 6713–6725. https://doi.org/10.1109/TGRS.2017.2731943

Knepp, D., & Houpis, H. (1991). ALTAIR VHF/UHF observations of multipath and backscatter enhancement. *IEEE Transactions on Antennas and Propagation*, *39*(4), 528–534. https://doi.org/10.1109/8.81467

Mannix, C. (2016). Measuring and modelling the impact of the ionosphere on space based synthetic aperture radars. Ph.D. dissertation, University of Birmingham, College of Engineering and Physical Sciences, Birmingham, U.K.

Mannix, C., Belcher, D., & Cannon, P. (2017). Measurement of ionospheric scintillation parameters from SAR images using corner reflectors. *IEEE Transactions on Geoscience and Remote Sensing*, *55*(12), 6695–6702. https://doi.org/10.1109/TGRS.2017.2727319

Meyer, F., Chotoo, K., Chotoo, S., Huxtable, B., & Carrano, C. (2016). The influence of equatorial scintillation on L-band SAR image quality and phase. *IEEE Transactions on Geoscience and Remote Sensing*, *54*(2), 869–880. https://doi.org/10.1109/TGRS.2015.2468573

Moreira, A. (2013). Synthetic aperture radar (SAR): Principles and applications. 4th Advanced Training Course in Land Remote Sensing. Athens, Greece.

Morton, Y., Xu, D., Carroll, M., Jiao, Y., Wang, J., Taylor, S., & Mao, X. (2014). Multi-constellation and multi-frequency GNSS studies of ionospheric scintillation. Radio Science Meeting (USNC-URSI NRSM), 2014 United States National Committee of URSI National. Boulder, CO: IEEE. https://doi.org/10.1109/USNC-URSI-NRSM.2014.6928060

Motohka, T., Isoguchi, O., Sakashita, M., & Shimada, M. (2018). ALOS-2 PALSAR-2 Cal/Val updates. JAXAe/EORC Joint PI Meeting of Global Environment Observation Mission FY2017.

Ningthoujam, R. K., Balzter, H., Tansey, K., Morrison, K., Johnson, S. C., Gerard, F., et al. (2016). Airborne S-band SAR for forest biophysical retrieval in temperate mixed forests of the UK. *Remote Sensing*, *8*(7), 1–22. https://doi.org/10.3390/rs8070609

Prikryl, P., Ghoddousi-Fard, R., Weygand, J. M., Viljanen, A., Connors, M., Danskin, D. W., et al. (2016). GPS phase scintillation at high latitudes during the geomagnetic storm of 17–18 March 2015. *Journal of Geophysical Research: Space Physics*, *121*, 10,448–10,465. https://doi.org/10.1002/2016JA023171

Priyadarshi, S. (2015). A review of ionospheric scintillation models. *Surveys in Geophysics*, *36*(2), 295–324. https://doi.org/10.1007/s10712-015-9319-1

Rao, P., Ram, S., Krishua, S., Niranjan, K., & Prasad, D. (2006). Morphological characteristics of L-band scintillations and their impact on GPS signals-a quantitative study on the precursors for the occurrence of scintillations. Meeting Proceedings RTO-MP-IST-056, (pp. 6(1)–6(22)). Neuilly-sur-Seine, France.

Rino, C. (1979). A power law phase screen model for ionospheric scintillation: 1. Weak scatter. *Radio Science*, *14*(6), 1135–1145. https://doi.org/10.1029/RS014i006p01135

Rino, C., & Fremouw, E. (1977). The angle dependence of singly scattered wavefields. *Journal of Atmospheric and Terrestrial Physics*, *39*(8), 859–868. https://doi.org/10.1016/0021-9169(77)90166-0

Rino, C. L., & Gonzalez, V. H. (1983). Propagation effects in satellite-borne synthetic aperture radars. In *Propagation factors affecting remote sensing by radio waves*, 345, 5-1 to 5-12, NATO-AGARD, Electromagnetic Propagation Panel (EPP), Oberammergau, Federal Republic of Germany, 18–24 May.

Rishbeth, H. (1971). Polarization fields produced by winds in the equatorial F region. *Planetary and Space Science*, *19*(3) 357–369. https://doi.org/10.1016/0032-0633(71)90098-5

Secan, J. A., Bussey, R. M., & Fremouw, E. (1995). An improved model of equatorial scintillation. *Radio Science*, *30*(3), 607–617. https://doi.org/10.1029/94RS03172

Seif, A., Abdullah, M., Hasbi, A., & Zou, Y. (2011). Observation of GPS ionospheric scintillation at UKM, Malaysia. IEEE International Conference on Space Science and Communication (IconSpace) (pp. 45–50). Penang, Malaysia: IEEE. https://doi.org/10.1109/IConSpace.2011.6015849

Shimada, M., Muraki, Y., & Otsuka, Y. (2008). Discovery of anomalous stripes over the Amazon by the PALSAR onboard ALOS satellite. IEEE International Geoscience and Remote Sensing Symposium (IGARSS) Boston, MA: IEEE. https://doi.org/10.1109/IGARSS.2008.4779009

Somayajulu, Y. V., Garg, S. C., Dabas, R. S., Singh, L., Tyagi, T. R., Lokanadham, B., et al. (1984). Multistation study of nighttime scintillations in low latitudes: Evidence of control by equatorial F region irregularities. *Radio Science*, *19*(3), 707–718. https://doi.org/10.1029/RS019i003p00707

Spatz, D., Franke, S., & Yeh, K. (1988). Analysis and interpretation of spaced receiver scintillation data recorded at an equatorial. *Radio Science*, *23*, 347–361. https://doi.org/10.1029/RS023i003p00347

Thébault, E., Finlay, C., Beggan, C., Alken, P., Aubert, J., Barrois, O., et al. (2015). International Geomagnetic Reference Field: The 12th generation. *Earth, Planets and Space*, *67*(1), 67–79. https://doi.org/10.1186/s40623-015-0228-9

Tong Minh, D. H., Toan, T. L., Rocca, F., Tebaldini, S., Vilard, L., Rejou-Mechain, M., et al. (2016). SAR tomography for the retrieval of forest biomass and height: Cross-validation at two tropical forest sites in French Guiana. *Remote Sensing of Environment*, *175*, 138–147. https://doi.org/10.1016/j.rse.2015.12.037

Vacchione, J., Franke, S., & Yeh, K. (1987). A new technique for estimating zonal irregularity drifts and variability in the equatorial F region. *Radio Science*, *22*(5), 745–756. https://doi.org/10.1029/RS022i005p00745

Van de Kamp, M., & Cannon, P. (2009). Spectra of equatorial total electron content derived from GPS signals. *Annales Geophysicae*, *27*(5), 2205–2214. https://doi.org/10.5194/angeo-27-2205-2009

Van de Kamp, M., Cannon, P., & Terkildsen, M. (2009). Effect of the ionosphere on defocusing of space-based radars. *Radio Science*, *44*, RS1003. https://doi.org/10.1029/2007RS003808

Wernik, A., Alfonsi, L., & Materassi, M. (2007). Scintillation modeling using in situ data. *Radio Science*, *42*, RS1002. https://doi.org/10.1029/2006RS003512

Whitney, H., Aarons, J., & Malik, C. (1969). A proposed index for measuring ionospheric scintillations. *Planetary and Space Science*, *17*(5), 1069–1073. https://doi.org/10.1016/0032-0633(69)90114-7

Xu, Z.-W., Wu, J., & Wu, Z.-S. (2004). A survey of ionospheric effects on space-based radar. *Waves in Random Media*, *14*(2), S189–S273. https://doi.org/10.1088/0959-7174/14/2/008